

Enhancing Fatigue Performance of Additively Manufactured Ti6Al4V – The Role of Surface Characteristics and Post-Processing Techniques

Andrzej Kurek^{1*}, Łukasz Źrodowski^{2,3}, Tomasz Choma^{2,3}, Izabela Abramczyk⁴,
Mariusz Kłonica⁵, Marcin Wachowski⁶

¹ Faculty of Mechanical Engineering, Opole University of Technology, Opole, Poland

² Faculty of Materials Science and Engineering, Warsaw University of Technology, Warsaw, Poland

³ Amazemet Sp. z o. o., Ltd., Al. Jana Pawła II 27, 00-867 Warsaw, Poland

⁴ Faculty of Mechanical Engineering, Bydgoszcz University of Technology, Bydgoszcz, Poland

⁵ Faculty of Mechanical Engineering, Lublin University of Technology, Lublin, Poland

⁶ Military University of Technology, Faculty of Mechanical Engineering, Warsaw, Poland

* Corresponding author's e-mail: a.kurek@po.edu.pl

ABSTRACT

3D printing technology proves itself to be effective in the field of medical industry due to processing potential of titanium alloys. Nonetheless it also has its drawbacks, the most severe being high roughness of printed elements' area as well as the need to remove support structures created following the printing. Mechanical processing is commonly used for said parameters being enhanced. The completion of that process, however, takes a lot of time and prevents hard-to-reach elements from being reached. The task of this article is to provide a new method of firming the print's surface and removing load-bearing structures. To achieve this, selective laser melting (SLM) technology will be used along with bathing prints in HF/HNO₃ solution, all of which are supported by ultrasound. This process will enhance the material fatigue processing while reducing the postprocessing time and complexity.

Keywords: additive manufacturing, SLM, fatigue life, surface finishing, TI-6AL-4V.

INTRODUCTION

Fatigue strength evaluation is a critical aspect of strength analyses, especially for structural components subjected to cyclic loading. This evaluation is essential for predicting the durability and lifespan of materials under repeated stress conditions. Tension-compression and oscillatory bending are the primary loading conditions used in fatigue testing, providing a comprehensive understanding of how materials behave under real-world operational stresses [1]. The results of these tests are typically represented in fatigue characteristics, which include both strain and stress parameters. These characteristics are pivotal for engineers and researchers as they inform design decisions and ensure the safety and reliability of structural

components [2]. Moreover, fatigue studies are integral to understanding crack initiation mechanisms, which are fundamental in predicting failure modes and improving material performance. The insights gained from fatigue strength evaluations not only enhance the theoretical framework of material science but also have practical implications in various industries, including aerospace [3], automotive [4, 5], and civil engineering [6, 7]. By delving into the fatigue properties of materials, researchers and engineers can develop more resilient and efficient structures, ultimately pushing the boundaries of modern engineering. In order to determine the fatigue strength on an element we need some kind of 'base line' to refer to. That 'base line' is fatigue characteristic (fatigue life curve) created on the basis of fatigue

tests on specimens performed in laboratories [8–10]. There are many different parameters that have an effect on final result, like load conditions [11, 12], but the surface condition of specimens is definitely among the most impactful on fatigue life [13–17]. This phenomenon is even more important with 3D printed complex shapes [18], like lattice structures [19]. We can distinguish several types of fatigue characteristics commonly used in the field, depending on the load conditions we can use stress-life models [20–22], strain-life models [23–25] or energy-based models like SWT [26].

To focus our investigation, we distinguished between stress-based (high cycle fatigue) and strain-based (low cycle fatigue) characteristics, selecting the stress-based approach for this study. We employed the Basquin S-N curve to conduct our tests, a widely recognized method despite the availability of numerous alternatives in the literature. The tests were performed under

tension-compression loading conditions to evaluate the material’s fatigue performance accurately.

EXPERIMENTAL DATA

Ti6Al4V alloy produced through additive manufacturing was subjected to three sets of fatigue tests to evaluate the influence of surface finishing on its fatigue strength. The specimen geometry is shown of Figure 1. These tests were performed using the state-of-the-art Instron ElectroPuls E10000 Linear-Torsion machine (Figure 2), which is designed for both dynamic and static testing. This advanced equipment allowed for precise tension-compression testing across a wide range of materials and components, which itself is a part of the Opole University of Technology’s Laboratory of Fatigue Life, Strength of Materials and 3D Printing Methods. In 1910, Basquin [21] proposed a fatigue diagram that

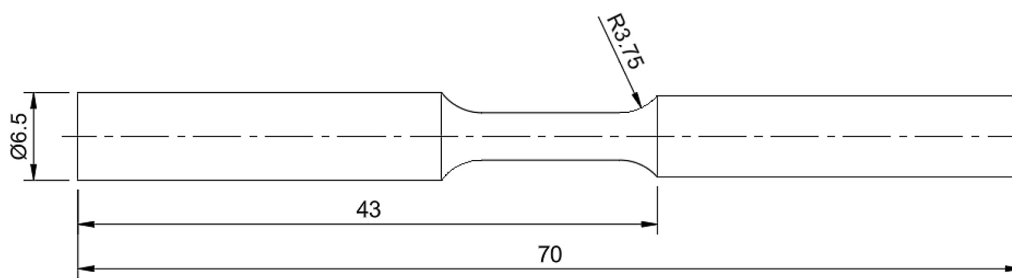


Figure 1. Test specimen geometry



Figure 2. Instron ElectroPuls E1000 test stand

illustrates the relationship between the number of cycles to failure and the stress amplitude on a double logarithmic scale $\log(\sigma_a)$. This diagram, along with a corresponding tension-compression equation, has become a foundational tool in fatigue analysis:

$$\sigma_a = \sigma_f'(2N_f)^b \quad (1)$$

where: N_f – being fatigue life in cycles, σ_a – tension-compression or bending stress amplitude and σ_f' – fatigue strength coefficient.

It may also be rewritten as:

$$N_f = A + m \log \sigma_a \quad (2)$$

where: both A and m are regression model constants.

Additively manufactured Ti6Al4V's characteristics differing in surface condition are shown on Figures from 3 to 11. 3 types can be distinguished:

- no surface postprocessing (machining) – Figures 3–5.
- HF/NHO3 bath assisted by ultrasound – Figures 6–8.

- mechanical postprocessing (machining) – Figures 9–11.

Figures 3, 6 and 10 represent the 2D map of specimen topography with a black line indicating reference for the roughness diagram for Figures 4, 7 and 9. While Figures 5, 8 and 11 are

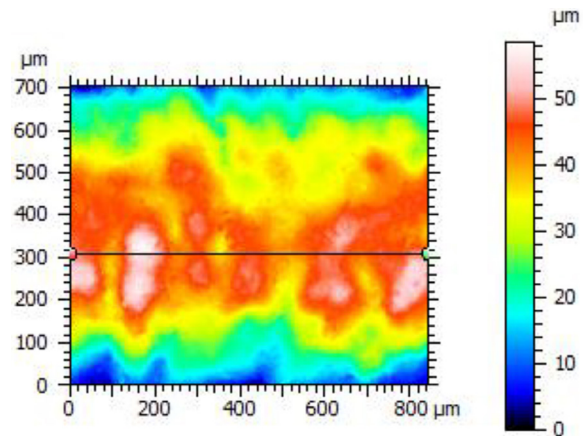


Figure 3. Optical micrograph shows non-polished specimen surface

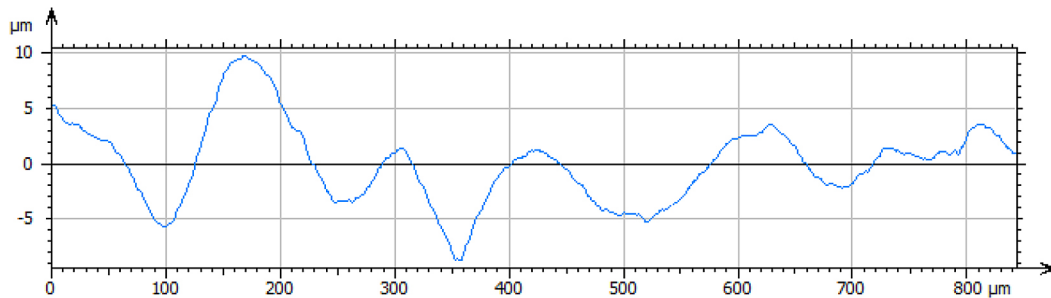


Figure 4. Roughness diagram of non-polished specimen surface

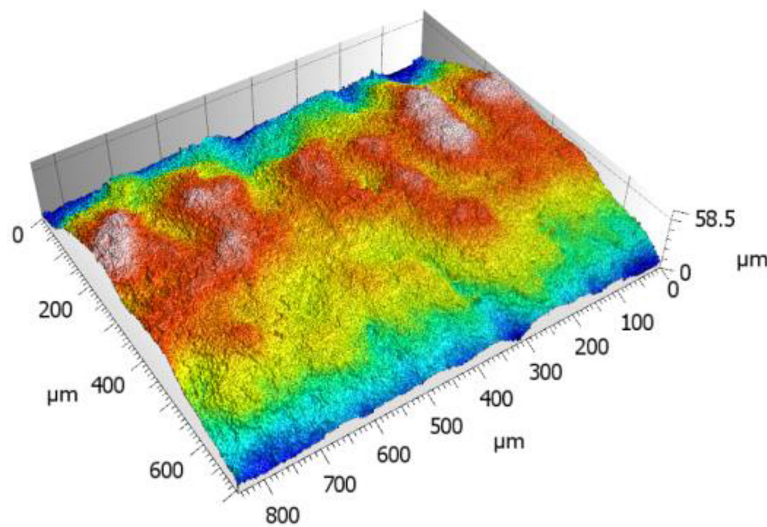


Figure 5. 3D Optical micrograph shows non-polished specimen structure

Table 1. The chemical composition Ti6Al4V as reported by the manufacturer

Ti	Al	V	Fe	O	C	N	Oth
Balance	6.55	4.15	< 5000 ppm	< 2000 ppm	< 800 ppm	< 500 ppm	0.1

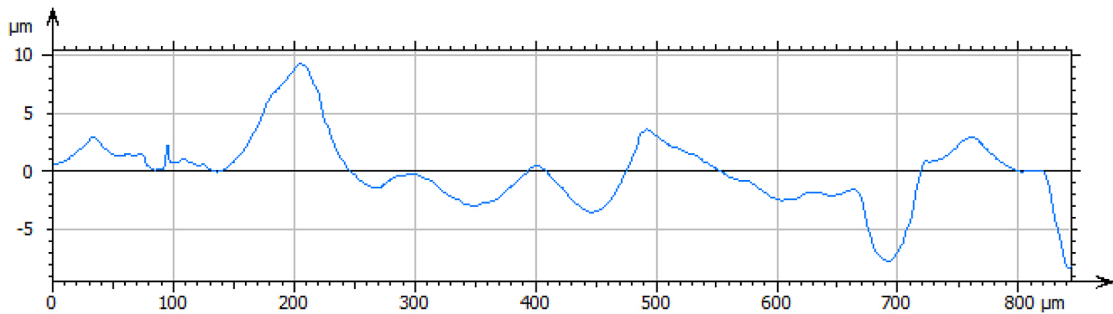


Figure 6. Roughness diagram of chemical polished specimen surface

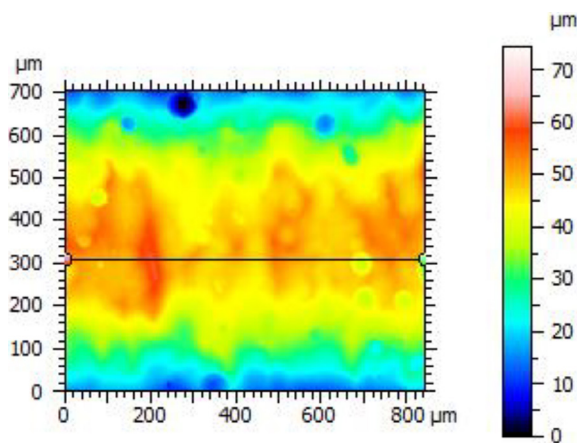


Figure 7. Optical micrograph shows chemical polished specimen surface

3D versions of said figures for no surface processing, HF/NHO3 bath assisted by ultrasound and mechanical postprocessing (machining) respectively.

MATERIALS AND METHODS

Materials

The fatigue specimens from Ti6Al4V were produced using an EOSINT M100 LPBF machine from EOS GmbH. The powder used had particle sizes specified as $d_{10} = 23 \mu\text{m}$, $d_{50} = 33 \mu\text{m}$, and $d_{90} = 46 \mu\text{m}$. The chemical composition of the

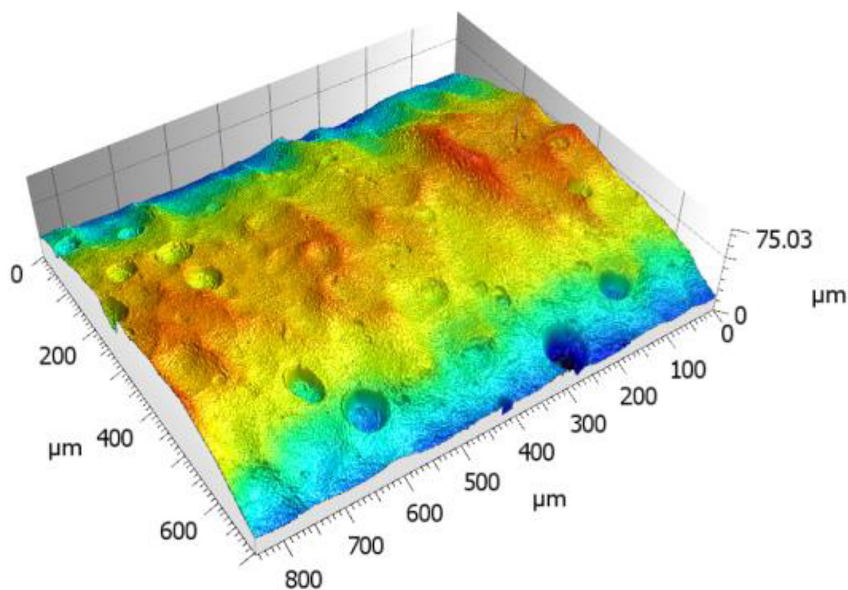


Figure 8. 3D optical micrograph shows chemically postprocessed specimen structure

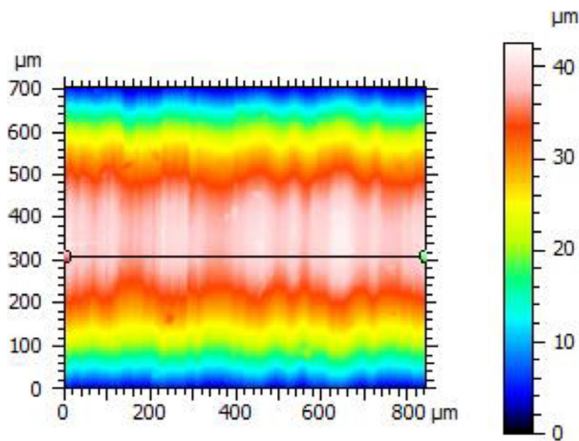


Figure 9. Optical micrograph shows mechanical polished specimen surface

material adheres to the ASTM F3001 international standard [27] and is presented in Table 1. All specimens were produced vertically, as that is the least favorable condition, in a building chamber

flooded with 5.0 argon shielding gas, so that the oxygen level would stay below 0.1%. The specimens were then removed from building plate and heat-treated. The heat-treatment was conducted in vacuum furnace at set temperature of 850 °C for the period of 1 hour.

Mechanical postprocessing

The diamond turning experiment was carried out using a fresh diamond tool and an ultraprecision machining device, the Moore Nanotech 350 FG, set at a 12.5° flank clearance angle. The gauge and final diameters of the specimens were measured with an analog caliper, offering an accuracy of ± 0.01 mm. The cutting process was performed at a speed of 80 m/min with a maximum cut depth of 0.3 mm. Surface roughness was measured following the completion of the cut to assess the finishing quality.

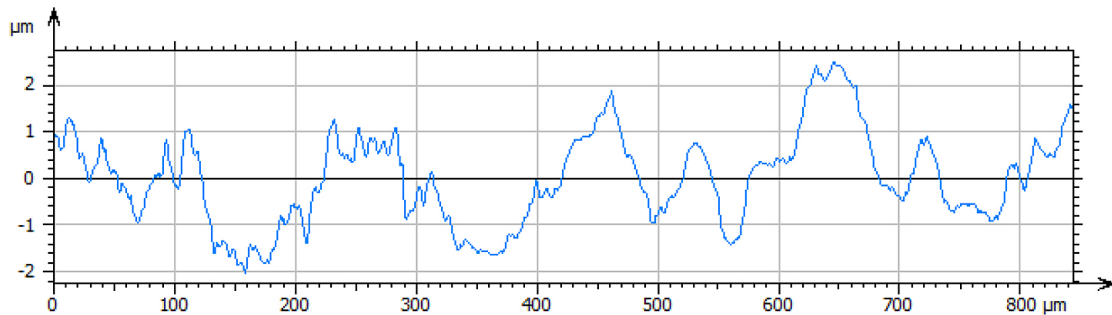


Figure 10. Roughness diagram of mechanical polished specimen surface

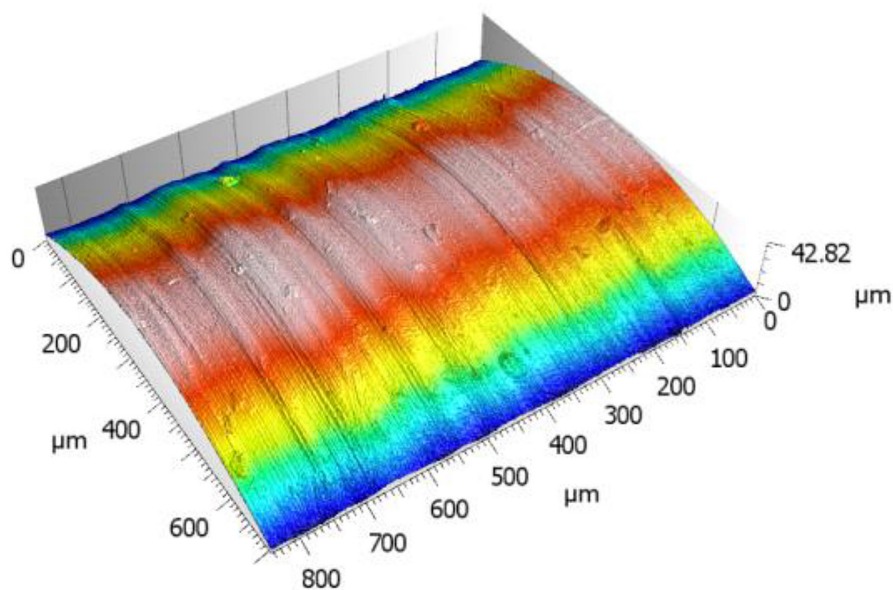


Figure 11. 3D optical micrograph shows mechanical polished specimen structure

Chemical postprocessing

To chemically post-process the alloy, a set of predefined solutions was used [7, 28], consisting of hydrofluoric and nitric acids [29] in a 2.0/20% mHF/HNO₃ ratio. The specimens were bathed in this solution for six minutes. Following the chemical treatment, both the gauge and final diameters were measured using the same analog caliper with an accuracy of ± 0.01 mm as described earlier.

Roughness measurement

Due to its significant impact on fatigue strength, profile roughness was evaluated in all specimens in accordance with ISO 4287 and ISO 25178 standards using a surface roughness profiler. A Mitutoyo Surftest 501, equipped with a probe tip radius of 5 µm, was employed for the linear evaluation of roughness. Additionally, surface roughness was measured through microscopic observations using a Sensofar 3DS profilometer both before and after mechanical post-processing.

TOPOGRAPHY AND SURFACE FINISHING

Without surface postprocessing

Surface roughness topology was analyzed to characterize the treated specimens. It is easily noticeable that lack of treatment caused the specimen's surface to be uneven and made the amplitude of surface gradation high, also distributing the peaks unevenly. The height difference ranged from 10 to -9 µm, exhibiting a sparse distribution pattern.

Chemical postprocessing

Using the chemical solution managed to smoothen the surface, however, it left several defects caused most likely by internal porosity,

leaving the print's surface less even than in case of mechanical postprocessing.

Figure 9 illustrates height differences ranging from 8 to -8.5 µm across the structure. The microstructure image reveals a consistently smooth surface on the specimen. This observation underscores the uniformity and precision achieved through the manufacturing process.

Mechanical postprocessing

Mechanical post-production yields a surface structure that is notably uniform and consistent. Unlike chemical postprocessing, which can exhibit larger height differences, mechanical methods result in smaller variations in surface height. Moreover, the influence of machining's axiality is clearly evident on the surface texture, reflecting the precision and directional characteristics of the machining process. This controlled approach not only enhances the aesthetic appearance of the material but also plays a crucial role in optimizing its mechanical properties, making it suitable for demanding applications where surface integrity is paramount.

Raw prints without any postprocessing have shown height differences four times larger than the postprocessed ones ranging from -2 to 2 µm. The density of height distribution was the highest of all studies. For each specimen type, 3 random specimens were measured. The summary of measured surface parameters for all three types of specimens can be found in Table 2, as averages of 3 measurements. For all measurements were done with a cut-off wavelength $\lambda_s = 2.5 \mu\text{m}$ and $\lambda_c = 0.25 \text{ mm}$.

MECHANICAL ANALYSIS

To accurately characterize the fatigue behavior of a material and construct a reliable SN (Wöhler)

Table 2. Surface parameters for tested specimens

Parameter	As print	Chemical postprocessing	Machined
R _p	4.11	3.95	1.53
R _v	4.86	3.41	1.29
R _z	8.97	7.36	2.82
R _c	8.04	4.45	1.82
R _t	12.13	10.92	3.12
R _a	2.15	1.42	0.61
R _q	2.51	1.89	0.72

curve, it is essential to test a significant number of specimens for each fatigue curve. In this study, 14 or 15 specimens were deemed sufficient to represent corresponding stress levels for each type of specimen. This extensive testing was necessary to capture the inherent variability in material properties, surface conditions, and experimental conditions, thereby ensuring statistical reliability and reproducibility of the results. Tables 3–6 and Figure 12 present the establishment of said tests. Groups of specimens are marked with different symbols. Table 3 show raw prints without surface smoothness interference. Table 4 contain the results of chemical postprocessing specimens. Mechanical postprocessing results are visible in Table 5.

Table 6 shows all SN curve coefficients, with all characteristics presented in Figure 12. All the data and Wöhler curves clearly show that element fatigue strength increases with smoothing of the specimens [30, 31]. Having been tested using the same stress levels it is, clearly and unsurprisingly, visible that mechanically processed prints have the highest fatigue strength thanks to their surfaces being the most consistent. Finding the postprocessing method with the lowest fatigue strength on the other hand proves itself to be difficult due to lack of an unequivocal result. All fatigue tests were conducted at a frequency (f) of 15 Hz and with no mean stress values, resulting in a stress ratio (R) of -1.

In Figure 12 all three methods have been compared showing that postprocessing of prints has a

great impact of fatigue life which compares with the literature [32]. The chemical treatment’s effect is shown in the middle and indicates fatigue resistance twice as big as in case of raw prints.

MICROSTRUCTURAL ANALYSIS

Metallographic studies were performed on Ti6Al4V specimens made using the sintering technique and subjected to different post-process processing. The macroscopic view of the

Table 4. Experimental data for specimens after chemical postprocessing

Name	σ_a , MPa	N_f , cycle
Ti_chem_1	365	62 635
Ti_chem_2	350	69 133
Ti_chem_3	340	142 277
Ti_chem_4	330	178 760
Ti_chem_5	320	296 141
Ti_chem_6	375	131 390
Ti_chem_7	390	53 801
Ti_chem_8	400	62 708
Ti_chem_9	310	389 529
Ti_chem_10	300	2 000 000
Ti_chem_11	450	35 758
Ti_chem_12	440	49 679
Ti_chem_13	360	89 604
Ti_chem_14	386	79 569
Ti_chem_15	340	11 235

Table 3. Experimental data for specimens without any surface postprocessing

Name	σ_a , MPa	N_f , cycle
Ti_as_print_1	450	19 902
Ti_as_print_2	430	27 114
Ti_as_print_3	415	43 117
Ti_as_print_4	400	28 167
Ti_as_print_5	315	71 441
Ti_as_print_6	300	83 934
Ti_as_print_7	285	171 609
Ti_as_print_8	270	173 534
Ti_as_print_9	255	135 523
Ti_as_print_10	240	2 000 000
Ti_as_print_11	245	144 633
Ti_as_print_12	350	50 426
Ti_as_print_13	360	39 640
Ti_as_print_14	375	33 456
Ti_as_print_15	290	11 236

Table 5. Experimental data for machined specimens

Name	σ_a , MPa	N_f , cycle
Ti_mach_1	346	412 400
Ti_mach_2	460	27 357
Ti_mach_3	470	33 057
Ti_mach_4	465	92 732
Ti_mach_5	460	51 194
Ti_mach_6	440	66 826
Ti_mach_7	430	178 303
Ti_mach_8	420	198 823
Ti_mach_9	410	193 692
Ti_mach_10	400	155 368
Ti_mach_11	400	342 440
Ti_mach_12	365	389 560
Ti_mach_13	426	118 600
Ti_mach_14	375	11 500

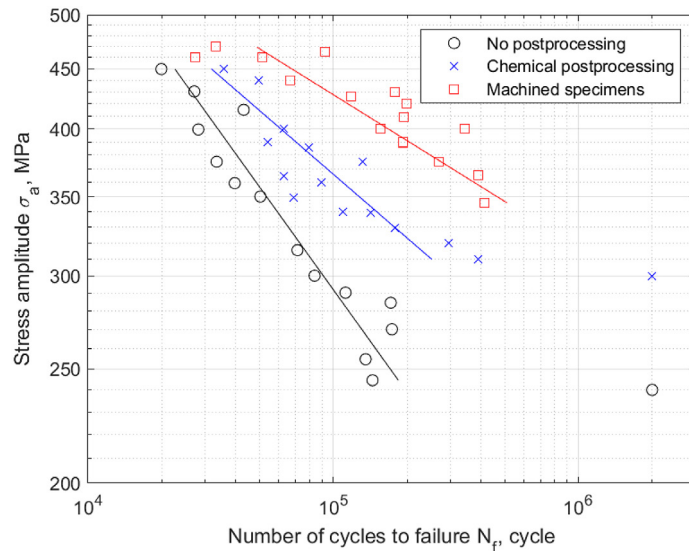


Figure 12. Wöhler diagram for tension-tension fatigue tests on Ti6Al4V specimens after three different surface finishing methods

Table 6. SN curve coefficients for all three types of specimens

Specimen type	Basquin regression model constants	
	A	m
As print	13.69	-3.53
Chemical postprocessing	18.82	-5.39
Machined	26.45	-8.14

chemical postprocessing specimens supplied for tests and the macroscopic image of the mechanical postprocessing specimens are presented in Figure 13 and Figure 14, respectively. The cross-sectional macrostructure of additively manufactured specimens is shown in Figure 13 and Figure 14 in longitudinal and transverse sections. While the microstructure of pores and trapped particles

can be better seen on Figure 15. In general, the microstructure of the specimen is dense. Powder inclusion in the monolithic mass are clearly visible, as well as Lack-of-Fusion (LoF) artifacts. Such structural defects are typical for L-PBF technology and occur due to the interaction of the laser beam with spatter contaminants formed during the process. Defects seem to place randomly within the whole volume of the specimens.

To further investigate this topic Computed Tomography (CT) has been prepared with a Phoenix V Tome xS volumetric scanner (Germany, Waygate Technologies) to obtain a model of the actual geometry of the specimens. The system consists of a 1000×1000 px (200 μm pixel size) 16-bit grayscale detector, a rotary table as well as a micro-focus X-ray tube with a maximum accelerating voltage of 240 kV. CT reconstructions

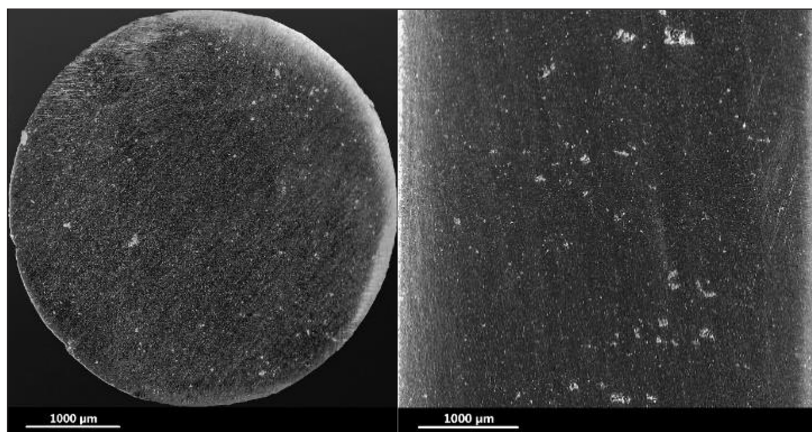


Figure 13. Metallographic view of chemical post processing

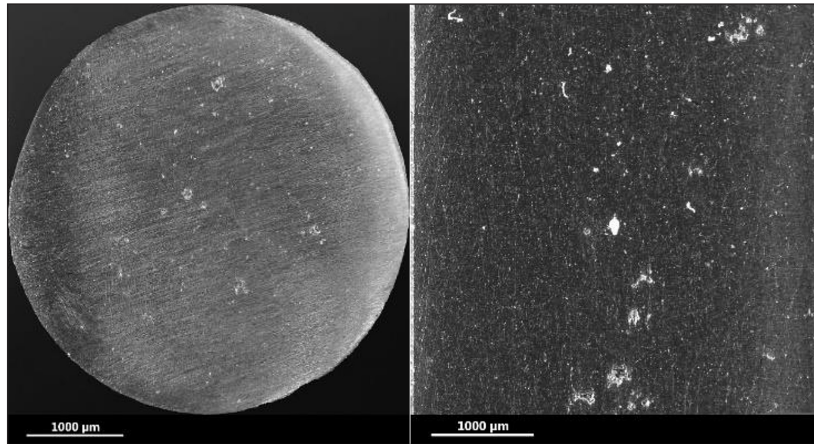


Figure 14. Metallographic view of mechanical post processing

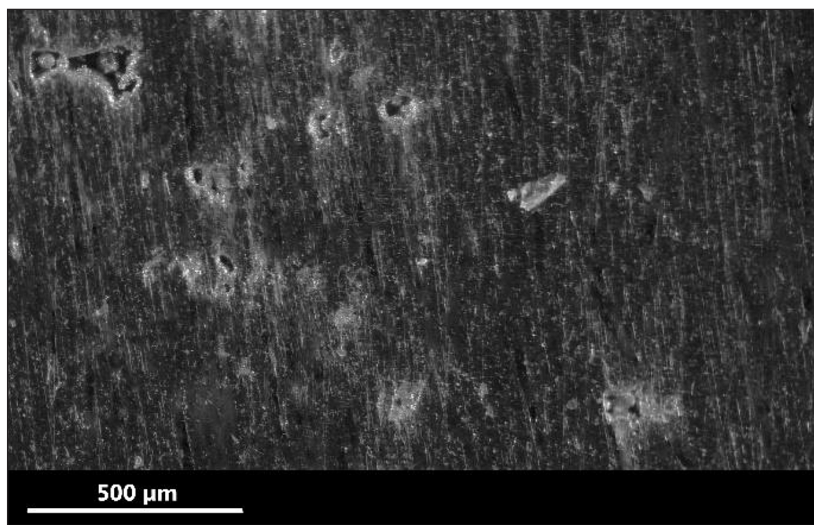


Figure 15. Microstructure of pores and trapped particles

are shown in Figures 16 to 18. Pores characteristic corresponds to metallographic analysis revealing a structure of LoF pores ranging from 100 μm to 600 μm at longest axis. Size of visible metal powder grains are about 40 μm diameter. The size of the irregularly shaped structural voids, with maximum dimension of 300 μm . The total pore capacity does not exceed 3% of the specimen volume. It seems that pores are located within the interior of the specimen and surface is rather defect-free. Such an effect could be contributed to so called skin-parameters involving re-melting of the specimen boundaries. The machined specimen (Figure 18) shows most pores, which further supports the assumption that the surface of the printed specimen was of better quality due to optimized surface countering parameters and with machining removing this layer of enhanced surface material, more pores occurs.

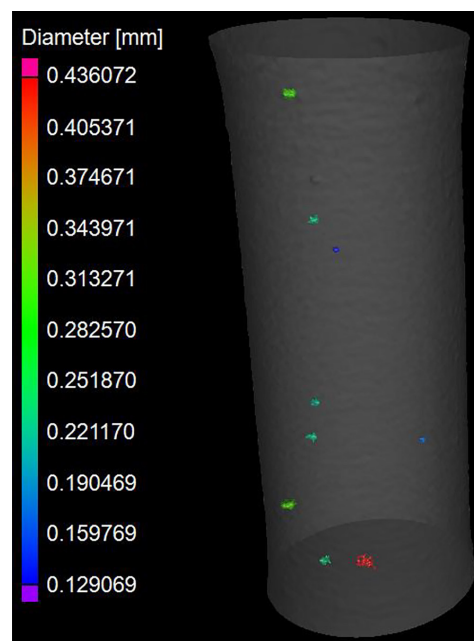


Figure 16. CT reconstruction of as-printed specimen

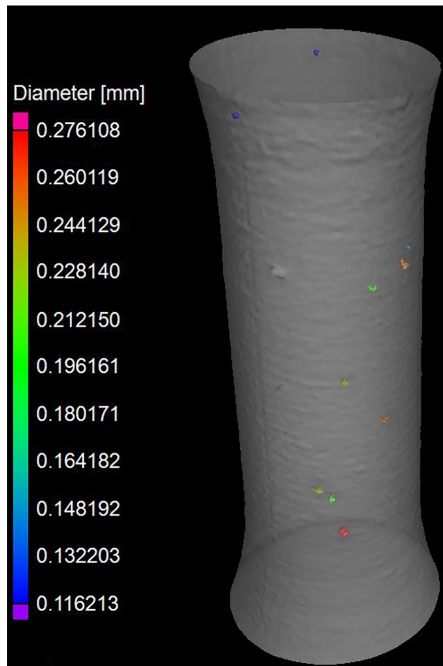


Figure 17. CT reconstruction of chemically postprocessed specimen

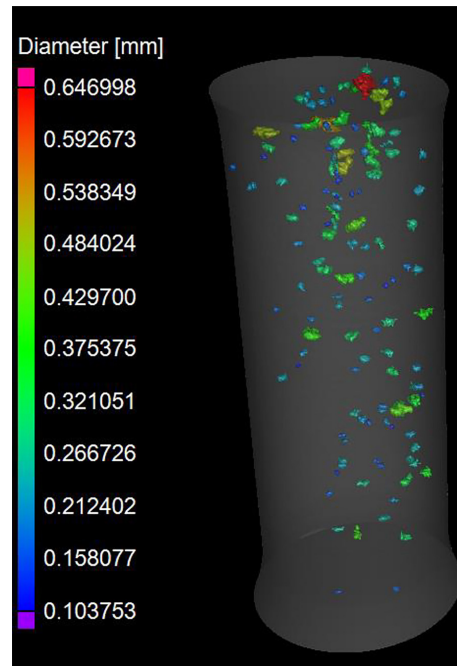


Figure 18. CT reconstruction of a machined specimen

CONCLUSIONS

Based on the experiments and tests conducted, several key conclusions can be drawn regarding the etching and postprocessing of 3D printed Ti6Al4V titanium alloy. These findings highlight significant improvements in both surface quality and mechanical properties:

- Achieving even etching on 3D printed titanium alloys is possible.
- Powder particles adhered to the surface can be removed through chemical postprocessing.
- Powder inside the structure can be removed using ultrasound.
- No mechanical properties are degraded by these processes.
- The specimen's fatigue limit is improved by the postprocessing.
- Processed specimens exhibited a fatigue life that was up to two times higher compared to as-printed conditions.
- While the process is indicated for simplified geometries, chemical postprocessing also allows for treatment of more geometrically complex objects, enhancing mechanical advantages in practical use.
- Additive Manufacturing benefits from this process, offering new guidelines for design and considering the fatigue limits of prints.

- Despite defects and large scatter in porosity between specimens, surface quality remains a predominant factor for the fatigue strength of L-PBFed material.

REFERENCES

1. Walczak M. Surface characteristics and wear resistance of 316L stainless steel after different shot peening parameters. *Adv Sci Technol J* 2023; 17: 124–32. <https://doi.org/10.12913/22998624/165800> WE - Emerging Sources Citation Index (ESCI).
2. Karolczuk A., Kurek M., Łagoda T. Fatigue life of aluminium alloy 6082 T6 under constant and variable amplitude bending with torsion. *J Theor Appl Mech* 2015; 53: 421–30. <https://doi.org/10.15632/jtam-pl.53.2.421>
3. Nagalingam A.P., Gopasetty S.K., Wang J., Yuvaraj H.K., Gopinath A., Yeo S.H. Comparative fatigue analysis of wrought and laser powder bed fused Ti-6Al-4V for aerospace repairs: Academic and industrial insights. *Int J Fatigue* 2023; 176. <https://doi.org/10.1016/J.IJFATIGUE.2023.107879>
4. Jin J.W., Kang K.W., Lee S. Fatigue analysis for automotive wheel bearing flanges. *Int J Precis Eng Manuf* 2023; 24: 621–8. <https://doi.org/10.1007/S12541-023-00773-Z>
5. Mikušová N., Badiarová S., Jeřábek K. Optimization of welding pliers production for the automotive industry—case study. *Adv Sci Technol Res J* 2020; 14: 240–9. <https://doi.org/10.12913/22998624/128105>

6. Skoczylas J., Kłonica M., Samborski S. A study on the FRP composite's matrix damage resistance by means of elastic wave propagation analysis. *Compos Struct* 2022; 297: 115935. <https://doi.org/10.1016/J.COMPSTRUCT.2022.115935>
7. Lyczkowska E., Szymczyk P., Dybała B., Chlebus E. Chemical polishing of scaffolds made of Ti-6Al-7Nb alloy by additive manufacturing. *Arch Civ Mech Eng* 2014; 14: 586–94. <https://doi.org/10.1016/J.ACME.2014.03.001>
8. Kulesa A., Kurek A., Łagoda T., Achteлик H., Kluger K. Low cycle fatigue of steel in strain controlled cyclic bending. *Acta Mech Autom* 2016; 10: 62–5. <https://doi.org/10.1515/ama-2016-0011>
9. Achteлик H., Kurek M., Kurek A., Kluger K., Pawliczek R., Łagoda T. Non-standard fatigue stands for material testing under bending and torsion loadings. *AIP Conf. Proc.*, AIP Publishing; 2018, 2029, 20001. <https://doi.org/10.1063/1.5066463>
10. Kurek M. Including the normal to shear stresses ratio in fatigue life estimation for cyclic loadings. *MATEC Web Conf* 2019; 300: 15005. <https://doi.org/10.1051/mateconf/201930015005>
11. Kowalski S. Failure analysis of the elements of a forced-in joint operating in rotational bending conditions. *Eng Fail Anal* 2020; 118. <https://doi.org/10.1016/J.ENGFAILANAL.2020.104864>
12. Kowalski S., Pexa M., Aleš Z., Čedík J. Failure analysis and the evaluation of forced-in joint reliability for selected operation conditions. *Coatings* 2021; 11. <https://doi.org/10.3390/COATINGS11111305>
13. Wei X., Alahmer A., Ali H., Tahat S., Vyas P.P., Hamasha S. Effect of temperature on the low cycle fatigue properties of BGA solder joints. *Microelectron Reliab* 2023; 146. <https://doi.org/10.1016/J.MICROREL.2023.115031>
14. Atzeni E., Genna S., Salmi A., Trovalusci F., Rubino G. Abrasive fluidized bed finishing of additive manufactured cobalt-chrome parts: effects on surface morphology and fatigue behavior. *Int J Adv Manuf Technol* 2023; 124: 1939–49. <https://doi.org/10.1007/S00170-022-10580-X>
15. Kurek A., Łagoda T., Kurek M. Stress gradient as a size effect in fatigue life determination for alternating bending. *Int J Fatigue* 2021; 153: 106461. <https://doi.org/10.1016/J.IJFATIGUE.2021.106461>
16. Kowalski S. Influence of diamond-like carbon coatings on the wear of the press joint components. *Wear* 2021; 486–487: 204076. <https://doi.org/10.1016/J.WEAR.2021.204076>
17. Kubit A., Macek W., Zielecki W., Szawara P., Kłonica M. Fracture surface topography parameters for S235JR steel adhesive joints after fatigue shear testing. *Adv Sci Technol Res J* 2023; 17: 130–9. <https://doi.org/10.12913/22998624/171490>
18. Mieloszyk J., Tarnowski A., Kowalik M., Perz R., Rządkowski W. Preliminary design of 3D printed fittings for UAV. *Aircr Eng Aerosp Technol* 2019; 91: 756–60. <https://doi.org/10.1108/AEAT-07-2018-0182/FULL/XML>
19. Moj K., Robak G., Owsinski R., Kurek A., Żak K., Przysiężniuk D. A new approach for designing cellular structures: design process, manufacturing and structure analysis using a volumetric scanner. *J Mech Sci Technol* 2022. <https://doi.org/10.1007/S12206-022-2107-1>
20. Kurek A., Kurek M., Łagoda T. Stress-life curve for high and low cycle fatigue. *J Theor Appl Mech* 2019; 57. <https://doi.org/10.15632/jtam-pl/110126>
21. Basquin O.H. The exponential law of endurance tests 1910; 10: 625–30.
22. Wöhler A.Z. *Bauwesen* 1858; 8: 642–52.
23. Manson S.S. Fatigue: A complex subject—Some simple approximations 1964: 193–226.
24. Kurek A., Kurek M., Łagoda T. Strain-life fatigue curves on the basis of shear strains from torsion. *Lect Notes Mech Eng* 2019: 395–402. https://doi.org/10.1007/978-3-030-04975-1_46
25. Coffin L.F.J. A Study of the Effects of Cyclic Thermal Stresses on a Ductile Metal. *Trans ASME* 1954; 76: 931–50.
26. Smith K.N., Watson P., A TTH. A stress-strain function for the fatigue of metals. *J Mater* 1970; 5: 767–78.
27. ASTM Standard F3001. Standard Specification for Additive Manufacturing Titanium-6 Aluminum-4 Vanadium ELI (Extra Low Interstitial) with Powder Bed Fusion. *ASTM B. Stand.*, 2014.
28. Truscello S., Kerckhofs G., Van Bael S., Pyka G., Schrooten J., Van Oosterwyck H. Prediction of permeability of regular scaffolds for skeletal tissue engineering: A combined computational and experimental study. *Acta Biomater* 2012; 8: 1648–58.
29. Sutter E.M.M., Goetz-Grandmont G.J. The behaviour of titanium in nitric-hydrofluoric acid solutions. *Corros Sci* 1990; 30: 461–76. [https://doi.org/10.1016/0010-938X\(90\)90051-6](https://doi.org/10.1016/0010-938X(90)90051-6)
30. Bagehorn S., Wehr J., Maier H.J. Application of mechanical surface finishing processes for roughness reduction and fatigue improvement of additively manufactured Ti-6Al-4V parts. *Int J Fatigue* 2017; 102: 135–42. <https://doi.org/10.1016/J.IJFATIGUE.2017.05.008>
31. Wysocki B., Idaszek J., Buhagiar J., Szlązak K., Brynk T., Kurzydłowski K.J., Świączkowski W. The influence of chemical polishing of titanium scaffolds on their mechanical strength and in-vitro cell response. *Mater Sci Eng C* 2019; 95: 428–39. <https://doi.org/10.1016/J.MSEC.2018.04.019>
32. Okuniewski W., Walczak M., Szala M. Effects of shot peening and electropolishing treatment on the properties of additively and conventionally manufactured Ti6Al4V alloy: a review. *Materials* 2024; 17(4): 1–29. <https://doi.org/10.3390/ma17040934>